2016

Mean characteristics of fluid structures in shallow-wake flows

Ram Balachandar
University of Windsor

International Journal of Multiphase Flow 82 (2016) 74–85

Contents lists available at ScienceDirect

International Journal of Multiphase Flow

journal homepage: www.elsevier.com/locate/ijmultiphaseflow

Mean characteristics of fluid structures in shallow-wake flows

G. Nasif*, R. Balachandar, R.M. Barron

Department of Mechanical, Automotive & Materials Engineering, University of Windsor, ON N9B 3P4, Canada

ARTICLE INFO

Article history:
Received 29 September 2015
Revised 20 December 2015
Accepted 1 March 2016
Available online 15 March 2016

Keywords:
Bluff body
Shallow flow
Fluid-structure interaction
3-D structures
VOF

ABSTRACT

An enhanced picture of the formation of fluid structures including the effect of the free surface and the bed is captured via a numerical solution of flow past a bed mounted bluff body. A numerical comparison for the fluid structures observed in a time-averaged field of the shallow-wake flow behind a bluff body utilizing the rigid-lid assumption and volume of fluid method is carried out in this study to bring forth the shortcomings in previous studies. The transient three-dimensional governing Navier–Stokes equations are computationally solved using a finite volume technique with Detached Eddy Simulation as a turbulence model. A flat wave model is used with the volume of fluid method to simulate the free surface of the water-air interface. The flow structures in the shallow-wake are qualitatively identified using the λ_2-criterion. In addition to the well-known features present in traditional shallow flows, other distinctive features are captured at the near-bed and near-surface locations. The formation of these structures and their dynamics are addressed in this paper. It is found that use of the volume of fluid method, which provides a more accurate representation of the free surface, has a significant impact on the structures' development at the near-surface location in the far-wake and on the streamtraces in front of the bluff body. Unique streamwise oriented structures are captured in the near-bed and free surface, which transport the fluid particles from the centre of the wake to the outer region. To the contrary, the fluid structures with the rigid-lid assumption are not completely developed near the free surface.

Introduction

Various flows taking place in nature and in many engineering applications can be considered to be shallow. In these flows, the length scale in the horizontal plane is much larger than the length scale in the vertical plane. Jirka and Uijttewaal (2004) defined the shallow flow as primarily horizontal and occurring in a vertically limited depth. If L and H are the typical horizontal and flow depth length scales, respectively, then the kinematic condition for shallow flow is described by $L/H \gg 1$. The other requirement for shallow flows is a dynamic condition, which entails at least one boundary that must be shear-supporting, e.g., the bottom of the channel. Shallow wakes occur when a shallow flow is destabilized by a sudden perturbation of topology, such as by introduction of a bluff body. The vertical shear in a shallow flow assists to deplete the flow energy and stabilize the wake flow. There are many practical situations which are regarded as shallow-wake flow, e.g., atmospheric flow around mountains, stratified flows such as flow around islands in oceans and lakes, tidal waves, etc. A better understanding of shallow-wake flows and their transport capability is important since this will facilitate better modelling of such flows. This would also assist in evaluating the dissipation of heat and dispersion of pollutants and biological species in the flow.

The bed effect can have a considerable impact on the flow characteristics in the shallow-wake flow. The stability parameter $S = C_f D/H$ is a measure of the strength of the bed friction, which accounts for the flow stabilization (Singha and Balachandar, 2011a). Here, D is the characteristic length of the bluff body and C_f is the bed skin friction. The vortex shedding from the sides of a bluff body might either suppress or become intermittent if the stability parameter goes beyond a critical value (Singha and Balachandar, 2010). The effect of the bed becomes weaker as one moves towards the free surface. At near-bed locations, the bed effect arrests the expansion of the wake, weakens the interaction between shear layers, and stabilizes the flow (Singha and Balachandar, 2011b).

Due to the computational complexity of modelling a free surface, very little computational work on shallow-wake flows has been performed until now. Most theoretical and numerical results of the shallow-wake flow have been obtained by considering the rigid-lid assumption. Previous studies have ignored the propagation of surface waves and focussed on processes that evolve more slowly without considering near-surface events (White et al., 2006). Nasif et al. (2015) numerically investigated the turbulence

* Corresponding author. Tel.: +1 519 2533000 x5407 +1 519 8192620; fax: +1 519 9737007.
E-mail address: nasifg@uwindsor.ca (G. Nasif).

http://dx.doi.org/10.1016/j.ijmultiphaseflow.2016.03.001
0301-9322/

structures that are present in a shallow-wake flow behind a bluff body using Detached Eddy Simulation (DES) as a turbulence model and utilizing the rigid-lid assumption. Distinctive flow features were revealed in this study, which was focused on the turbulent structures at the near-bed location. A pair of two-dimensional spiralling patterns resembling the owl face of the first kind was identified at locations two to three diameters downstream of the bluff body. These patterns are stable at locations close to the bed, while their rotational sense switches from stable inward to unstable outward as they moves towards the free surface. A pattern initiated directly downstream of the bottom of the bluff body was also revealed by Nasif et al. (2015). This pattern represents a section through a structure that arises from a horizontally oriented secondary roll-up process in the centre of the near-wake region. The well-known horseshoe structure was also captured at the near-bed location, this structures resides at the bed and extends downstream along the sides of the bluff body. Additionally, a collar vortex was captured by Nasif et al. (2015); this structure is buried in a high vorticity region at the near-bed location and emerges from both sides of the bluff body. Perry and Steiner (1987) and Akilli and Rockwell (2002) previously reported both the owl face and roll-up structures. The above structures play a significant role in the development of the shallow-wake and provide the three-dimensional signature of the flow. Additional details about these structures can be found in Nasif et al. (2015).

Near the free surface, the turbulent kinetic energy in the vertical direction has been shown to be reorganized in the horizontal plane. This kinetic energy is associated with the upward flow which originates from the bed and is directed towards the free surface due to the three-dimensionality of the wake flow. The reorganization of kinetic energy happens in two independent fluid layers near the free surface (Hunt and Graham, 1978). The first layer is where the turbulent kinetic energy in the vertical direction reduces and the surface parallel component is increased. The second layer coincides with a very thin viscous layer, where the turbulent oscillation of the vertical velocity dies out and quickly reduces to zero. Walker et al. (1996) approximated the thickness of the previous and latter layers by one and one-tenth of the turbulent length scale, respectively. The energy reorganization is restricted to only large-scale structures of the flow, whereas the small-scale structures preserve their universality (Walker et al., 1996). Based on these observations, a numerical model of the free surface has been suggested by Shen et al. (2000) using a Large Eddy Simulation (LES).

Direct numerical simulation of the open channel flow was carried out by Pan and Banerjee (1995) to explore the large-scale structures appearing at the free surface. This investigation classified the structures into three classes: vortices, upwelling and downdraft. These types of structures have also been reported by Gupta et al. (1994) based on experimental observations. Vortices refer to the region of cluster of surface-normal vorticity where the ratio of surface-normal to the streamwise velocity is almost zero, i.e., the vertical velocity towards the free surface is insignificant. Upwelling is a region of deviation of streamlines with high surface-normal velocity. The downdraft region shows a strong downward velocity component which arises from the free surface. The surface-normal velocity has to be zero at the free surface; the above-mentioned surface-normal velocities occur at a very small region under the free surface.

Generally, there are two types of structures that can be detected close to the free surface; surface-normal structure tubes with predominantly vertical vorticity components and streamwise vortex tubes buried inside the surface layer. The structures and dynamics of turbulent wakes and shear layers in the presence of a free surface have been experimentally investigated by Maheo (1999) using particle image velocimetry. A pair of the surface-parallel tube structures, which have counter-rotating streamwise vorticity, is revealed beneath the free surface by time averaging of the flow-normal cross-section. These structures evolve away from each other but stay located at the edges of the wake, carrying low momentum fluid outwards from the wake central plane and widening the surface shear flow region at downstream locations. The widening of the turbulent shear layer at the near-surface can be as much as 20% for a turbulent wake (Maheo, 1999). These streamwise vortex tubes were found to produce surface currents, which affect the dynamics of the flow and distort the free surface.

The concept of vorticity and the definition of a vortex are very useful in the situation of turbulent flow, such as shallow-wake flow. The properties of turbulent shear flow are dominated by the performance of spatially coherent vortical motion called coherent structures. Jeong and Hussain (1995) hypothesized that the turbulence itself can be sufficiently described in a frame of interrelated vortex filaments. However, one key difficulty for the understanding of turbulent processes is the lack of an accepted description of what constitutes a vortex. There is almost consensus about the important properties as to what the vortex concept should include. Firstly, from a kinematic viewpoint, the vortex fluid particles rotate around a common centre or core. Secondly, the turbulent structure has a net vorticity, thereby excluding irrotational structures. This description of vortex implies Galilean invariance, meaning that the structure remains unchanged under the transformation of the shape. Thirdly, the rotation of the particle entails the presence of the centrifugal force that must be balanced against any combination of the pressure gradient, friction force, and change in the flow velocity. The core of the vortex can be described for example by a local minimum in the pressure field, if the effect of friction is small enough and the temporal turbulent scale of the motion is large (Jeong and Hussain, 1995).

In the context of a vortical description of the turbulent flow, one can expect that the attributes of coherent structures in the instantaneous flows, i.e., high vorticity, rotation around the core and pressure minima, also describe sufficiently these structures in the time-average flow (Rubinat, 2007). However, the definition of coherent structures in the average flow is essentially different from that in the instantaneous flow. The coherent structures in the non-averaged flow are constituted by real fluid particles with a rotational motion, while the structures are born out from the averaged characteristics in the mean flow.

Various methods have been recently adopted to detect the coherent structures. The absence of an accepted comprehensive description of a vortex translates into a multitude of principles that specify the existence of structures. The backgrounds of the different approaches that are currently used in the identification of coherent structures are discussed by Jeong and Hussain (1995) and Chakraborty et al. (2005), e.g., the velocity field and streamlines method, swirling strength method, pressure minima (λ_2-criterion), eigenvalues of the velocity gradient tensor (Q-criterion), etc. Both Q and λ_2-criteria are the most popular approaches that are currently used in the identification of the turbulent flow structures. The preference of using the λ_2-criterion over the Q-criterion to identify fluid structures is explained in Jeong and Hussain (1995), e.g., the latter approach does not assure the existence of pressure minima inside the region. The λ_2-criterion is based on the local analysis of the velocity gradient tensor. In this method, the centrifugal force applied outwards to the fluid particle due to the rotational or swirling motion must be balanced by an inward pressure gradient. The vortex axis is characterized by pressure minimum bounded by a region with a fairly strong pressure gradient. The λ_2-criterion proposed in Jeong and Hussain (1995) captures the pressure minimum in a plane normal to the vortex axis and accurately describes the vortex core at low and high Reynolds number. This criterion is derived based on the idea that

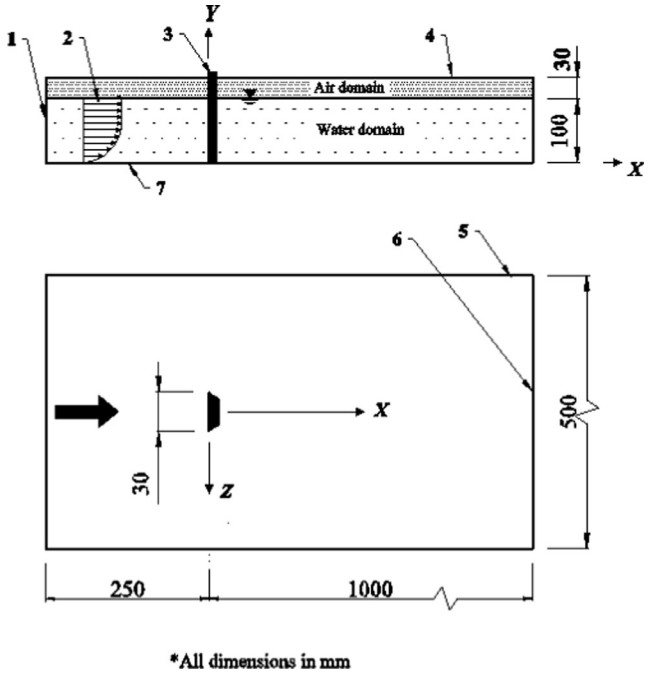

Fig. 1. Schematic of the flow with relevant boundary conditions.

a local pressure minimum in a plane fails to identify vortices under strong unsteady and viscous effects. By eliminating the effect of viscosity and unsteadiness, the symmetric part of the gradient of the incompressible Navier–Stokes equation can be written as:

$$\mathbf{S}^2 + \Omega^2 = -\frac{1}{\rho}\nabla(\nabla p) \tag{1}$$

where the left-hand side of Eq. (1) represents the symmetric tensor of the acceleration gradient, here $\mathbf{S}$ and Ω are symmetric and antisymmetric parts of the velocity gradient tensor $\nabla\mathbf{u}$, defined as:

$$\mathbf{S} = \left[\nabla\mathbf{u} + (\nabla\mathbf{u})^{\mathbf{T}}\right] \tag{2}$$

$$\Omega = \left[\nabla\mathbf{u} - (\nabla\mathbf{u})^{\mathbf{T}}\right] \tag{3}$$

The right hand side of Eq. (1) is a symmetric tensor representing the pressure Hessian. The vortex core was defined in Jeong and Hussain (1995) as a connected region with two positive eigenvalues of the pressure Hessian tensor (region of pressure minimum in a plane). If the eigenvalues of the tensor $\mathbf{S}^2 + \Omega^2$ are organized as $\lambda_1 \geq \lambda_2 \geq \lambda_3$, then this description is equivalent to the requirement that $\lambda_2 < 0$ at every point inside the vortex core. The equilibrium condition between centrifugal force and pressure gradient in the λ_2-criterion suggests that the flow is steady and inviscid. Therefore, the effectiveness of this method is related to the degree that the flow validates these conditions.

The objective of the current study is to determine the structures in the near-surface region and investigate their formation. The volume of the fluid method is employed to resolve the water-air interface at the free surface. It should also be noted that detailed fluid structures in the near-surface region could not be resolved properly in our previous numerical study (Nasif et al., 2015) due to the employment of the rigid-lid assumption to model the free surface. In addition, new findings relevant to the near-bed structures are addressed in this paper. In the current study, a shallow-wake flow is generated by introducing a vertical sharp-edged plate in a shallow open channel flow. The approaching flow separates at the sharp edges at all vertical distances from the bed. A three-dimensional time-dependent detached eddy simulation is used as a turbulence model in the study. Available data from previous PIV experiments (Singha and Balachandar, 2010; Singha and Balachandar, 2011a, b), are used to validate the computational results.

Model setup

A schematic diagram of the flow, comparable to the experimental setup in Singha and Balachandar (2010) and Singha and Balachandar (2011a, b), is shown in Fig. 1. The fully-developed turbulent boundary layer profile which is used as an inlet boundary condition is extracted by conducting a separate simulation. In this separate simulation, a two-phase flow model is used to simulate the flow in a 10.0 m long open channel with a depth of 0.13 m without any perturbation. The water depth in the channel is $H = 0.1$ m, while air occupies the rest of the space. The velocity profile at the exit of the 10.0 m long channel is employed as an approaching flow at the inlet boundary in the current study. This profile compares well with the experimental data and also conforms to the near-wall and universal log-law equations as shown in Fig. 2a and b, respectively.

The sharp-edged plate, which is employed as a bluff body, has a width $D = 0.03$ m. The plate was adjusted to be attached and vertical to the bed as shown in Fig. 1. A sharp-edged plate was chosen to assure that the boundary layer separates consistently at all vertical locations and to reduce the sensitivity to flow Reynolds number. It is worth mentioning that increasing the size of the bluff body will increase the scale of eddies and act to satisfy the generally accepted condition to denote a shallow wake, but it also creates other issues such as increasing blockage effects, etc. From the

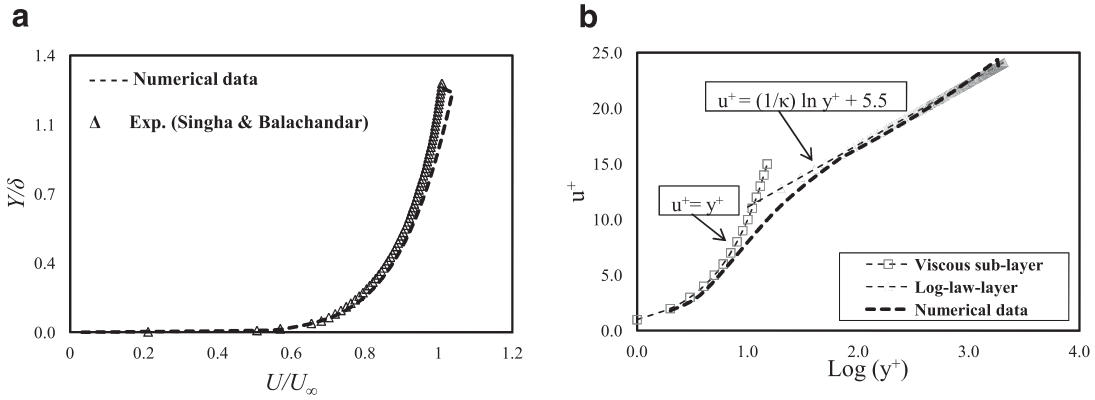

Fig. 2. (a) Mean streamwise velocity profile of the approaching flow from experiment and simulation; (b) Comparison of the numerical prediction of mean velocity profile with the universal law of wall.

authors' point of view, as long as the boundary layer thickness and the water depth are of the same order of magnitude, the flow can be deemed to be shallow. The wake vortices are constrained from growing in the vertical direction while they are unrestrained in the transverse direction.

The water and air physical properties are assumed constant and evaluated at 20 °C. The wall shear stress and friction velocity in the unperturbed flow are evaluated to be $\tau_w = 0.35$ Pa and $u^* = 0.019$ m/s, respectively. The boundary layer thickness δ constitutes 80% of the water depth. The free-stream velocity is $U_\infty = 0.44$ m/s and the turbulence intensity in the approaching flow is 2%. It was observed that the free-stream velocity with the two-phase flow simulation dropped slightly near the surface in comparison with the flow simulation using the rigid-lid assumption. This may be attributed to the shear stress at the interface between water and air. The maximum streamwise velocity, $U_{\max} = 0.45$ m/s, was found below the free surface. The Reynolds number value is calculated based on the bluff body width and the free-stream velocity as $\mathrm{Re} \approx 13{,}200$. The corresponding skin friction coefficient is found to be $C_f = 1.15 \times 10^{-3}$. The stability parameter based on this skin friction and water depth is estimated to be $S < 0.001$. Therefore, the Karman vortex street flow mode is expected to occur (Chen and Jirka, 1995). The slip condition is used to model the channel top surface, which is in contact with the air region, and the sidewalls of the computational domain, while the channel bottom is modelled as a non-slip boundary condition. The hydrostatic pressure of the flat wave model (explained in the next section) is used as a boundary condition for the pressure, while the outflow boundary condition is used for the velocity at the outlet.

The criteria for choosing the cell count in the current study are based on our earlier study (Nasif et al., 2015), i.e., the numerical results for many grids and many parameter settings were checked and compared with experimental results. The final cell count, which is employed to mesh the current computational domain shown in Fig. 1 (water and air regions) is 25×10^6 elements with cell sizes ranging between 5×10^{-5} and 4.0×10^{-3} m. The cell count in this study exceeds that of our previous study (Nasif et al., 2015), which utilized the rigid-lid assumption, by about 10%. The coarsest parts of the mesh are placed in the air region. Six layers of fine prism cells, packed in a 1.0 mm width with a stretching factor of 1.5, are employed to resolve the wall effect. The non-dimensional wall-normal distance is $y^+ < 3.0$. The cells are also clustered along the water-air interface to reduce the numerical diffusion and preserve the sharpness of the interface. Different time steps were attempted to satisfy the Courant-Friedrichs-Lewy (CFL) condition required for the implicit time step (see next section). The time step for the simulation is taken as 1×10^{-3} s with twenty internal iterations at each time step. The mean quantities from the simulation are calculated by averaging the transient results over a predefined time period of 60 s in the current study.

Computational approach

The shallow-wake flow is simulated using CD-adapco's STAR-CCM+ (2013) with a trimmer mesh. The trimmer meshing model utilizes a template mesh that is constructed from hexahedral cells from which it cuts or trims the core mesh using the starting input structured hexahedral surface mesh (CD-adapco's STAR-CCM+, 2013). First-order implicit marching in time and second-order differencing in space are used to discretize the governing equations. The governing equations for the transient analysis include a time-dependent conservation of mass equation and three time-dependent conservation of momentum equations. Each of these equations can be expressed in a general form by the transport of the appropriate scalar quantity ϕ, described in a continuous integral form as (Versteeg and Malalasekera, 1995):

$$\frac{\partial}{\partial t}\int_{\mathrm{CV}} \rho\phi dV + \oint_A \mathbf{n}\cdot(\rho\phi\mathbf{u})dA = \oint_A \mathbf{n}\cdot\left(\Gamma_\phi \nabla\phi\right)dA + \int_{\mathrm{CV}} S_\phi dV \quad (4)$$

where CV in Eq. (4) represents the three-dimensional control volume (cell) over which the volume integration is carried out, A is the bounding surface of the control volume and the surface integration is carried out over the entire surface of the CV. The terms in Eq. (4) from left to right are the rate of change of the total quantity of the fluid property ϕ in the control volume, the rate of change of the property ϕ due to the convection flux across the bounding surface of the control volume, the rate of change the property ϕ due to the diffusive flux across the bounding surface of the control volume, and the volumetric source in the control volume. The unit vector $\mathbf{n}$ in Eq. (4) is the outward normal vector to the surface element dA, $\mathbf{u}$ is the instantaneous velocity vector, ρ is the density and Γ_ϕ is the diffusion coefficient.

The flow in the current study involves two fluids, i.e., water and air, therefore a numerical model is required to handle the two-phase flow. The volume of the fluid (VOF) method (Hirt and Nichols, 1981) is a simple but powerful method based on the idea of a fractional volume of fluid in the control volume. This method is shown to be more flexible and efficient than other methods for treating complicated free-boundary problems (Hirt and Nichols, 1981). In VOF, the various fluids are assumed to share common properties at the interface. The solutions are obtained by solving the same set of basic governing equations as in a single-phase flow for an equivalent fluid whose physical properties are calculated as functions of the physical properties of its constituent phases and their volume fractions in the control volume. In the VOF method, an extra equation is required to transport the volume fraction of primary fluid α. This equation is described in the form of Eq. (4) with no source term and by setting $\phi = \alpha$ and $\Gamma_\phi = 0$.

The key task in the VOF method is to discretize the convective term in a way that avoids the artificial smearing of the interface. This is because all conventional schemes fail to approximate large spatial variations of the phase volume fraction. The high-resolution interface capturing (HRIC) scheme (Muzaferija et al., 1998), which utilizes the normalized variable diagram (Leonard, 1991), is used in the present simulation to discretize the convective term. In high-resolution schemes, an additional condition is required to satisfy the local Courant-Friedrichs-Lewy (CFL) condition. The CFL condition is a necessary condition for stability while solving certain partial differential equations. The value of local Courant number changes with the method that is used to solve the discretized equations, especially depending on whether the method is explicit or implicit. If an explicit time marching solver is used, then typically, a Courant number of less than one is required. Implicit solvers are usually less sensitive to numerical instability and so larger values of Courant numbers may be tolerated.

In the current study, the first-order flat wave model is used to simulate the surface gravity waves on the light fluid–heavy fluid interface. A first-order flat wave model represents a calm plane of water which has a periodic, sinusoidal motion only, i.e., it only specifies the direction and amplitude of the waves in the flow. This model is designed for three-dimensional cases, and is used with the volume of fluid multiphase model in STAR-CCM+ software (CD-adapco's STAR-CCM+, 2013). It provides a field function option that can be used to initialize the VOF calculation and prescribe suitable profiles at the boundaries, such as hydrostatic pressure at the channel outlet in Fig. 1.

In order to include and account for the effect of turbulence in the flow field, DES has been used as a turbulent model. A DES model is a hybrid model that attempts to couple the best features of the Reynolds-Averaged Navier-Stokes (RANS) and the large eddy

simulation (LES) methodologies in a single solution approach. In this technique, where the turbulent length scale is less than the maximum grid size, i.e., at near solid boundaries, the RANS mode is assigned for solution. When the turbulent length scale exceeds the size of the grid, i.e., at regions away from the solid boundaries, the turbulence model switches to LES mode to solve these regions. Therefore, the grid size requirements are less demanding than in a pure LES approach. The $k-\omega$ *SST* model (Menter, 1993 , 1994) is used as the RANS model within the DES simulation, where k is the turbulent kinetic energy, which determines the energy of the turbulence, and ω is the specific dissipation rate, which determines the scales of the turbulence. The shear stress transport (*SST*) model employs the $k-\omega$ formulation in the sub-layer viscous region and all the way down to the wall. Therefore, this model can be used as a low Reynolds number turbulence model without any further damping considerations. The $k-\omega$ *SST* model also switches to a $k-\varepsilon$ performance at a distance away from the wall and therefore avoids a common problem that is associated with the $k-\omega$ model, i.e., the sensitivity to free-stream turbulence properties. A delay factor introduced by Menter (2004) has been adopted in the DES formulation of the $k-\omega$ *SST* model. This modification enhances the ability of the model to distinguish between RANS and LES regions on computational meshes. The mathematical model of the DES formulation is outlined in the STAR-CCM+ User Manual (2013). The parameters Δ, l_t, C_{des} are used to characterize the delay parameter and introduce the transition between RANS and LES regions. Here Δ is the largest distance between the cell centre under consideration and the cell centres of the neighbouring cells, l_t is the length scale $(l_t = \sqrt{k}/0.09\omega)$, C_{des} is the model constant which blends the value obtained from independent calibration of the $k-\varepsilon$ and $k-\omega$ branches of the $k-\omega$ *SST* model (Travin et al., 2002). More details are available in the STAR-CCM+ User Manual (2013) for the evaluation of the delay factor and switching criteria between RANS and LES regions.

A segregated flow solver is used to solve the discretized equations according to a SIMPLE-type algorithm. The segregated flow solver controls two additional solvers; the velocity solver, which solves the discretized momentum equation to obtain the intermediate velocity field and the pressure solver, which solves the discretized equation for pressure correction and updates the pressure field. Based on the selected time step, the ratio of the shortest integral time scale in the near-wake region to the time step is approximately 2.0. The convective Courant number in the entire domain does not exceed one. In the current study, the computational results are considered to have converged when the continuity and momentum scaled residuals fall below 10^{-6}.

Validation

Validation is the procedure used to assure that the computational model is able to generate satisfactory and reliable results. This entails several aspects including correct physical representation of the problem, appropriate numerical schemes and accuracy of the model predictions. Extensive validations were demonstrated in our previous studies (Nasif et al., 2014, 2015), which utilized the rigid-lid assumption. Various wake characteristics were obtained numerically from these investigations, i.e., mean and statistical features. The numerical results were compared at three different elevations from the bed with the experimental results reported in Singha and Balachandar (2010) and Singha and Balachandar (2011a, b). The comparisons showed good agreement with the experimental results.

In the current study, the rigid-lid assumption is no longer used. Instead two regions, i.e., water and air, have been employed to handle the two-phase flow simulation and the cells are clustered at the water-air interface to prevent the numerical diffusion associated with the VOF model and to capture the free surface appropriately. Except for these modifications, all other parameters are kept unchanged as in the earlier study (Nasif et al., 2015). Therefore, one may expect that the previous validations, which were carried out using the rigid-lid assumption, will still be valid for the two-phase domain shown in Fig. 1. Nevertheless, additional validations are carried out in the present study by comparison with experimental results.

The development of the streamwise mean velocity U from the numerical simulation is extracted at the mid-depth plane $(Y/H = 0.5)$ at three downstream locations from the bluff body, i.e., $X/D = 1.0,\ 2.0$ and 3.0. This velocity is normalized by the maximum approaching stream velocity $(U_{max} = 0.45\,\mathrm{m/s})$ and compared with the corresponding experimental results as shown in Fig. 3. Both numerical and experimental velocity profiles in this figure appear nearly symmetrical about the wake central plane at $Z/D = 0.0$ and the numerical results are obviously in good agreement with the ones acquired from the experiment. Fig. 3 clearly reveals that at the wake central-plane, the streamwise velocity decreases and then increases as one moves from $X/D = 1.0$ to $X/D = 2.0$ and from $X/D = 2.0$ to $X/D = 3.0$, respectively at the mid-depth plane. This issue was well addressed in terms of the deficit velocity in Nasif et al. (2014).

Results

This study focuses on the fluid structures which are present in the mean flow field of the shallow-wake. Therefore, all mean quantities have to be calculated from the transient flow field data. The physical time that is used for averaging the transient quantities should be greater than the vortex-shedding period (here we assume that $t_{av}/T > 100$, where t_{av} and T represent the physical time used for averaging and the vortex-shedding period, respectively). Considering the time history of the transverse component at any location in the wake region, the frequency and vortex-shedding period can be calculated. In the present simulation, the temporal evolution of the transverse velocity component at a predefined point located three body widths downstream (Patil and Tiwari, 2008) at the horizontal mid-depth plane, i.e., at $Y/H = 0.5$, was computed with a time step $\Delta t = 0.001\,s$. As the shed vortices travel downstream, the transverse velocity of the fluid particles in the downstream of the wake fluctuates about zero mean value. Knowing the time history of the waveform, the Fast Fourier Transform (FFT) is used to calculate the frequency spectra of velocity. The frequency $f = 1.96/s$ defines the dominant and highest frequency in this figure, while the others are less dominant. Existence of such frequencies corresponds to small changes in the periodic nature of the velocity fluctuation, which may be related to the separation of small-scale vortices from the shear layers. The highest frequency corresponds to the vortex-shedding period $T = 0.51$ s. The time of 60 s is used for data averaging, which yields $t_{av}/T > 100$. The distinct sharp peak in the spectra characterizes the Strouhal frequency. Based on the width of the bluff body and the maximum streamwise velocity, the Strouhal number is $\mathrm{St} = 0.13$.

Comparison between VOF and rigid-lid assumption

One of the disadvantages of the rigid-lid assumption, which is frequently used, is the absence of the free surface (water–air interface). In fact, the free surface topology has a significant impact on the flow characteristics of the shallow-wake and thus its effect should be considered in the simulation to acquire improved results. Fig. 4 shows basic comparisons between the rigid-lid assumption and VOF simulations. The rigid-lid results are shown in the left hand side of the figure while the VOF results are in the right hand side.

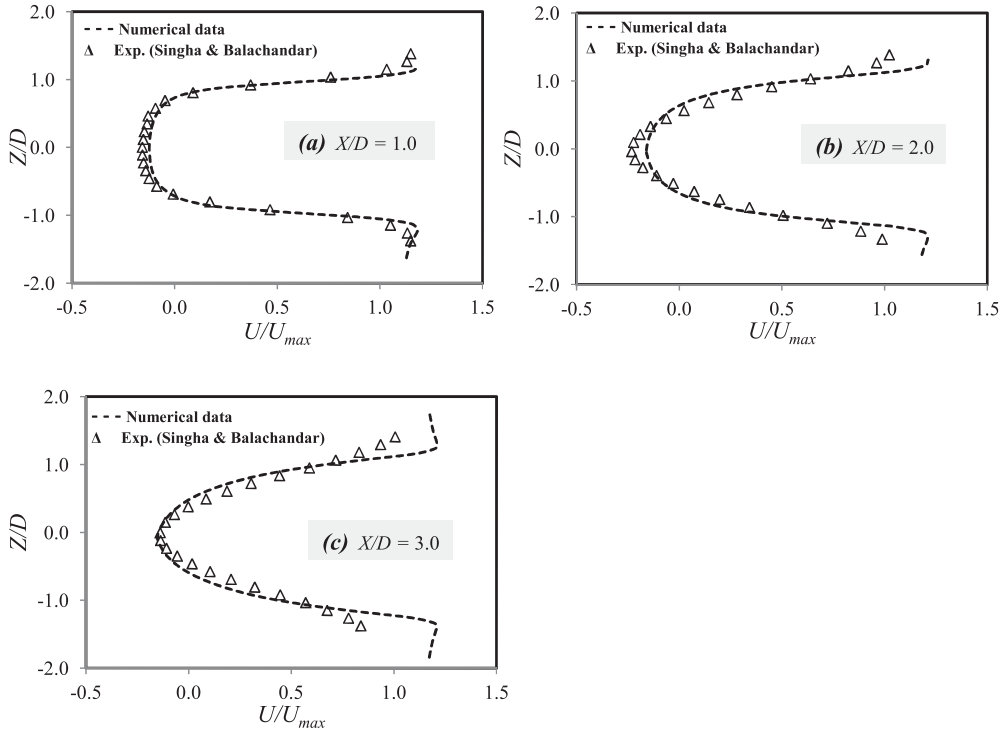

Fig. 3. Development of the streamwise mean velocity at downstream locations $X/D = 1.0$, 2.0 and 3.0 on the horizontal plane $Y/H = 0.5$.

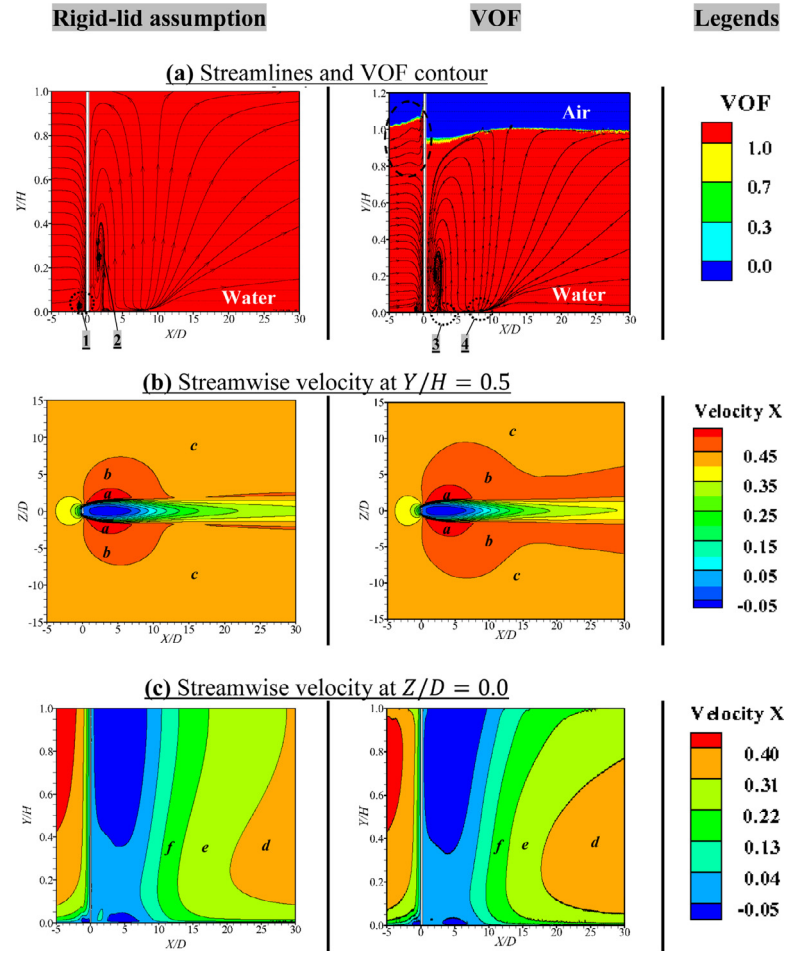

Fig. 4. Comparison between rigid-lid assumption and VOF simulation; (a) streamtraces and VOF contours; (b) streamwise velocity in the horizontal plane $Y/H = 0.5$; (c) contours of streamwise velocity in the vertical plane $Z/D = 0.0$.

Fig. 4a shows the time-averaged streamtraces superimposed by contours of VOF at the wake central plane, i.e., at vertical plane $Z/D = 0.0$. Here, streamtraces represent the projection of the 3-D streamlines on a given plane, i.e., a cross-section through the 3-D streamlines at $Z/D = 0.0$. Therefore, only two mean velocity components (U and V) are employed to extract the streamtraces in Fig. 4a. The upward flow from the bed is predominant through the wake central plane as shown in Fig. 4a. This flow provides the three-dimensional signature of the shallow-wake.

The well-known horseshoe vortex and 3-D roll-up structure, marked as Nos. 1 and 2, respectively, are captured in both sections of Fig. 4a. These structures were discussed in Nasif et al. (2015) and Akilli and Rockwell (2002). The 3-D roll-up structure is connected from each of its bottom sides to other structures (marked as No. 3) at the near-bed location. These structures, which have a distinctive three-dimensional feature, are identified on both sides of the wake central plane at $X/D \approx 2.75$. The expression "3-D bulged structure" was used previously in Nasif et al. (2015) to describe these structures. These structures are not clear in Fig. 4a because the slice is extracted at the wake central plane; however, its streamwise location is marked as No. 3 in the figure. More elaborate discussion is provided in the following section.

Another distinct feature marked as No. 4, which appears as a nodal point or source-like structure, is identified at $X/D \approx 8.0$ at the near-bed location in Fig. 4a. The locus of this nodal point represents the location where the streamtraces bifurcate to the right (downstream) and to the left (upstream) towards the bluff body. The presence of this node is attributed to the rollup of spanwise shear layers that sweep across the central plane at $Z/D = 0.0$ (Wang and Zhou, 2009). Generally, the streamtraces appear comparable in both sections of Fig. 4a. However, there is a major difference in the streamtraces topology observed in the front of the bluff body. In the rigid-lid assumption, all streamtraces are pointed downwards, which indicates there is always a downward flow towards the bed in front of the bluff body. However, in the VOF method, the streamtraces bifurcate at the vertical location $Y/H = 0.8$, which indicates there is a downward flow towards the bed for $Y/H < 0.8$ and upward flow towards the free surface for $Y/H > 0.8$ in front of the bluff body.

Contrary to the rigid-lid assumption, waves are captured in the free surface with the VOF simulation. At the wake central plane, i.e., vertical plane at $Z/D = 0.0$, a trough and peak in the water free surface are shown immediately behind and in front of the bluff body, respectively, as shown in Fig. 4a (right column). Fig. 4b shows the time-averaged streamwise velocity contours extracted in the horizontal plane $X/D = 0.5$. It is clearly shown in this figure that the outer accelerating flow region (the contour labelled as b, with the second highest velocity level) is wider and further stretched downstream with the VOF method in comparison with the rigid-lid assumption. This may be attributed to the presence of the aforementioned trough region. The trough region acts to reduce the flow cross-sectional area and due to continuity considerations, increases the size of the specified velocity contour. Generally, and for both approaches, the size of contour b increases as one moves towards the free surface where the bed effect becomes weaker. It is worth mentioning that using the VOF approach in the simulation provides a model that is closer to reality and hence should provide a better representation of the structures at the near-surface location. The structures at the near-surface are allowed to be developed further due to the additional interaction with the accelerating flow, i.e., with the velocity represented by the contour b in Fig. 4b (right column).

Fig. 4c shows the time-averaged streamwise velocity contours extracted in the wake central plane. The extent of both contours ranges between $0 \leq Y/H \leq 1.0$. The sections in Fig. 4c reveal that there is a very slight difference in the distribution of the streamwise velocity in the wake central plane. The deviation is only apparent in the three contour levels, which possess the highest velocity levels, i.e., contours d, e, and f in Fig. 4c.

Three-dimensional structures

In this section, the λ_2-criterion is used to identify the different structures in the mean flow. The λ_2-criterion was also used in our previous investigation (Nasif et al., 2015) to identify the turbulent structures in the transient flow. Fig. 5 illustrates the structures in the mean flow shaded by the streamwise vorticity component. These structures are shown for both the VOF method (Fig. 5a) and the rigid-lid assumption (Fig. 5b). The structures at the water-air interface associated with the VOF method are not shown in Fig. 5a for better illustration. The right-hand rule is used to conclude the rotational sense of the vorticity vector. Close inspection of Fig. 5 divulges that the wake flow includes different types of fluid structures.

A horseshoe vortex is very distinct in Fig. 5 and marked as No. 1. This structure is generated due to the interaction between the approaching flow, the bed, and the bluff body. It originates at about one body diameter upstream of the bluff body, wraps around it and stretches downstream as a pair of tube-like structures. The tube structures, which have a counter-rotating sense, contribute to the 3-D characteristics of the wake and enhance the entrainment process between the wake and its surroundings. The tubes of the horseshoe vortex are separated by five body diameters in the far-wake region and they are very similar in both approaches used in the simulations as shown in Fig. 5a and b. A collar structure marked as No. 9 in Fig. 5 has been discussed in detail in Nasif et al. (2015). The collar vortex emanates from the edges of the bluff body and is buried in a region of high vorticity in the near-bed location. These structures have the same rotation sense as the horseshoe vortex.

Another structure can be extracted from the mean flow, marked as No. 5 in Fig. 5. This structure occupies a significant portion of the wake region. It represents the averaging of the large-scale Karman vortex in the transient flow field, appears in the mean flow as a pair of counter-rotating tube structures normal to the free surface, and extends up to the downstream location where the recirculation region (a region with negative streamwise velocity) ends at $X/D \approx 8.0$, i.e., up to the nodal point in Fig. 4a. This structure interacts considerably with the accelerating mean flow and the bed due to two different factors. On the one hand, the kinetic energy is extracted from the mean flow and is fed to the structure by interaction with the lateral shear layer. On the other hand, in the boundary viscous layer, the kinetic energy that is extracted by the structure is depleted to the bed due to the wall shear stress. Therefore, the kinetic energy from the mean flow substitutes the loss of the kinetic energy due to the bed friction. The balance in the kinetic energy creates and maintains the structures marked as No. 5 in Fig. 5 up to the downstream location at $X/D \approx 8.0$.

At downstream locations $X/D > 8.0$, the kinetic energy is no longer sufficient to sustain the large-scale structures (marked as No. 5 in Fig. 5). This is attributed to the shortage in the kinetic energy due to the decrease of the mean velocity of the surroundings at locations $X/D > 8.0$ (see velocity contours a and b in Fig. 4b). Furthermore, the flow kinetic energy is less at elevations close to the bed compared to elevations near the surface. All previous factors act to decay the structures near the bed and progressively weaken the interaction between the structures (No. 5) and the bed as one moves downstream. The vertical tube structures are lifted and finally detached from the bed. As a result, new structures are seen to emerge from the structures marked as No. 5, aligned with the mean flow and stretched downstream. These new horizontal tube structures marked as No. 6 in Fig. 5, comprised of two parallel

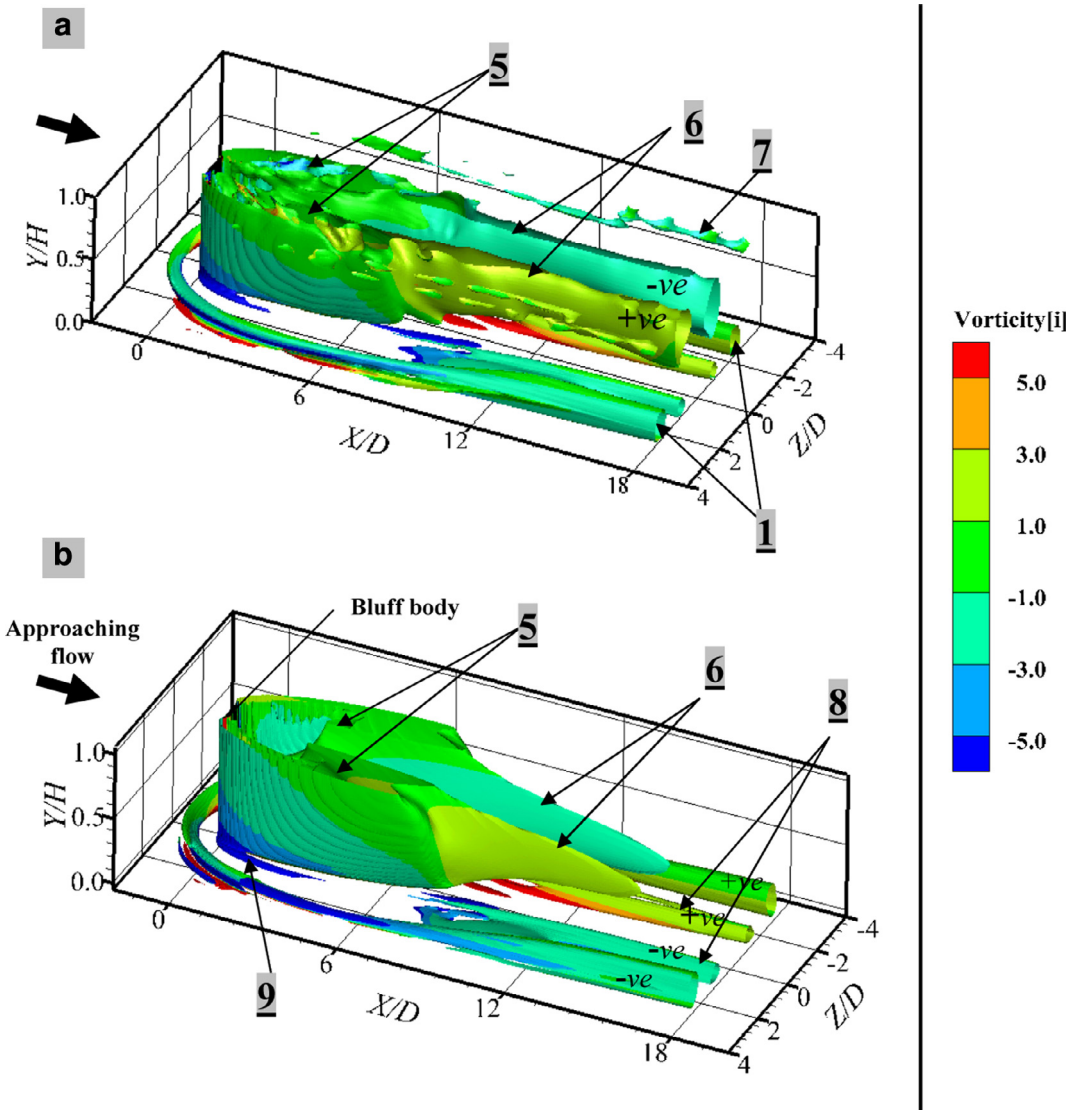

Fig. 5. Time-averaged λ_2 isosurface ($\lambda_2 = -1.0$) shaded by X-vorticity vector component from; (a) VOF method; (b) rigid-lid assumption.

counter-rotating tubes, are separated by two body diameters and located at approximately 1.25 body diameters below the surface.

More insight into the structures marked as No. 5 and 6 in Fig. 5 can be obtained by combining Fig. 4b and Fig. 5, as shown in Fig. 6. The domain in this figure is shown up to vertical location $Y/H > 0.6$ for better illustration. The level of the contour legends (coloured lines) for the streamwise velocity and vorticity in Fig. 6 are kept similar to the ones in the contours of Fig. 4b and Fig. 5, respectively. The structure marked as No. 5 is fed with the kinetic energy by the adjacent accelerating mean flow region, i.e., the contour with highest mean velocities level marked with the letter a in Fig. 6. As one moves farther downstream, the contour level of the mean velocity reduces to the level shown as contour b. Consequently, the kinetic energy that is transferred to the wake region declines and the structure marked as No. 6 is produced at the vertical location $Y/H > 0.45$.

In the rigid-lid assumption, an additional contour with less velocity level (marked as c) is observed at downstream location in Fig. 6b adjacent to the horizontal tube structures. This contour appears due to the absence of the aforementioned trough region associated with the VOF method. As a result, the energy transferred from the adjacent accelerating region (region c) to the wake region is not enough to sustain and maintain the structure marked as No. 6 in Fig 6b. The deficiency in the kinetic energy will terminate the structure No. 6 at a downstream location closer to the bluff body in the rigid-lid assumption in comparison with the VOF method. This observation is very obvious in Fig. 6a and b and demonstrates a clear distinguish between the rigid-lid assumption and the VOF method.

Other structures marked as No. 8 can be identified in Fig. 5. These structures include two parallel counter-rotating tubes that reside near the bed, originate at $X/D \approx 10.0$, and stretch downstream in the inner region adjacent to the horseshoe legs (No. 1 in Fig. 5) and below the horizontal tube structures (No. 6 in Fig. 5). These structures have the same rotational sense as the horseshoe vortex and an opposite rotational sense to that of the horizontal tube structures; the dynamics of its formation is affected by these structures, i.e., by structures No. 1 and 6 in Fig. 5.

More insight into the characteristics of structure No. 8 can be gained by extracting the fluid features at a specified downstream location as shown in Fig. 7. In this figure, the 2-D velocity vector along with the streamtraces superimposed by the streamwise vorticity contour is extracted at the streamwise location $X/D \approx 12.0$. The dotted line in Fig. 7 represents the edges of the fluid structures that are extracted by using the predefined λ_2-criterion. It is clearly shown in this figure that the upward flow is pre-

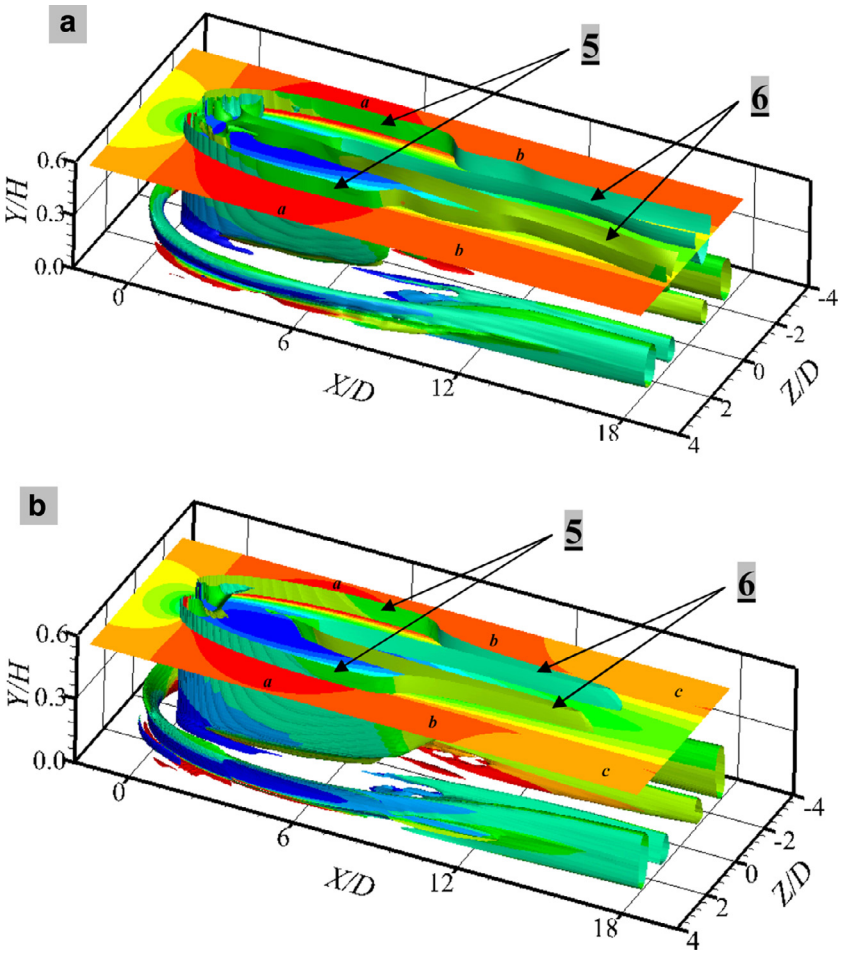

Fig. 6. Time-averaged λ_2 isosurface ($\lambda_2 = -1$) shaded by X-vorticity vector component with the streamwise velocity contour at horizontal plane $Y/H = 0.5$ from; (a) VOF method; (b) rigid-lid assumption.

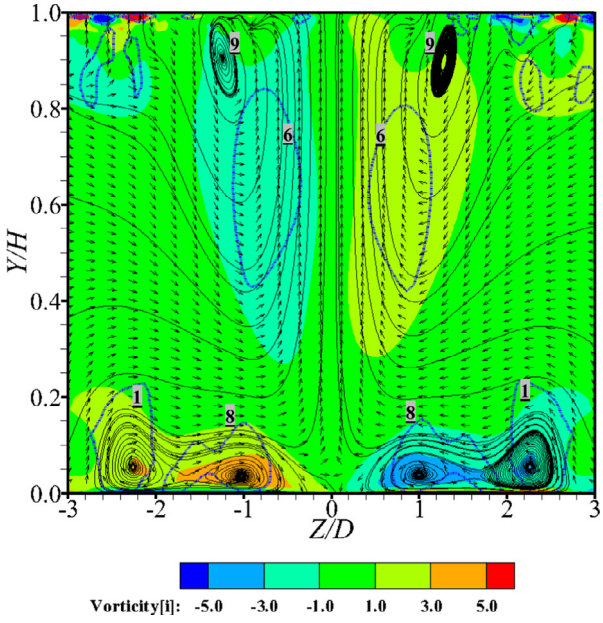

Fig. 7. Time-averaged streamtraces superimposed by a contours of the mean streamwise vorticity extracted at vertical plane $X/D = 12.0$. The dotted blue lines represent the border of the mean structures from the λ_2-criterion at $X/D = 12.0$. (For interpretation of the references to color in this figure legend, the reader is referred to the web version of this article.)

dominant at the wake central plane through the structure No. 6. However, at locations downstream of the nodal point (structure No. 4 in Fig. 4a), a downward flow is observed in a narrow region near the bed (see Figs. 4a and 7). The counter-rotation sense of both the horseshoe vortex (structure No. 1) and the horizontal tube structures (structure No. 6) enhance the entrainment between the surroundings and the core of the wake. The entrainment also assists to substitute the fluid that moves upwards through the wake central plane. Therefore, the fluid particles, which are driven into the wake region, stretch the horseshoe vortex inwards as shown in Fig. 7. As a result, the tube structures marked as No. 8 are established near the bed at one body diameter in the inner region near the horseshoe tubes. These tubes appear only in the far-wake region at downstream locations $X/D > 10.0$, because the presence of the vertical tube structures (structure marked as No. 5 in Fig. 5) inhibits this process in the near- and mid-wake regions. These structures diminish downstream as the entrainment process declines downstream.

The upward fluid flow impinges the free surface and diverges outwards away from the wake central plane. Therefore, new surface-parallel structures are established, i.e., structures marked as No. 9 in Fig. 7. The fluid particles on the wake boundary that move downwards to the bed due to the entrainment process and the existence of the structures marked as No. 6 will enhance the formation of these structures at the outer edges of the wake. They are initiated at a downstream location $X/D > 10.0$ near the free surface and stretch downstream in the far-wake. A section through these structures shows patterns which have the same rotational

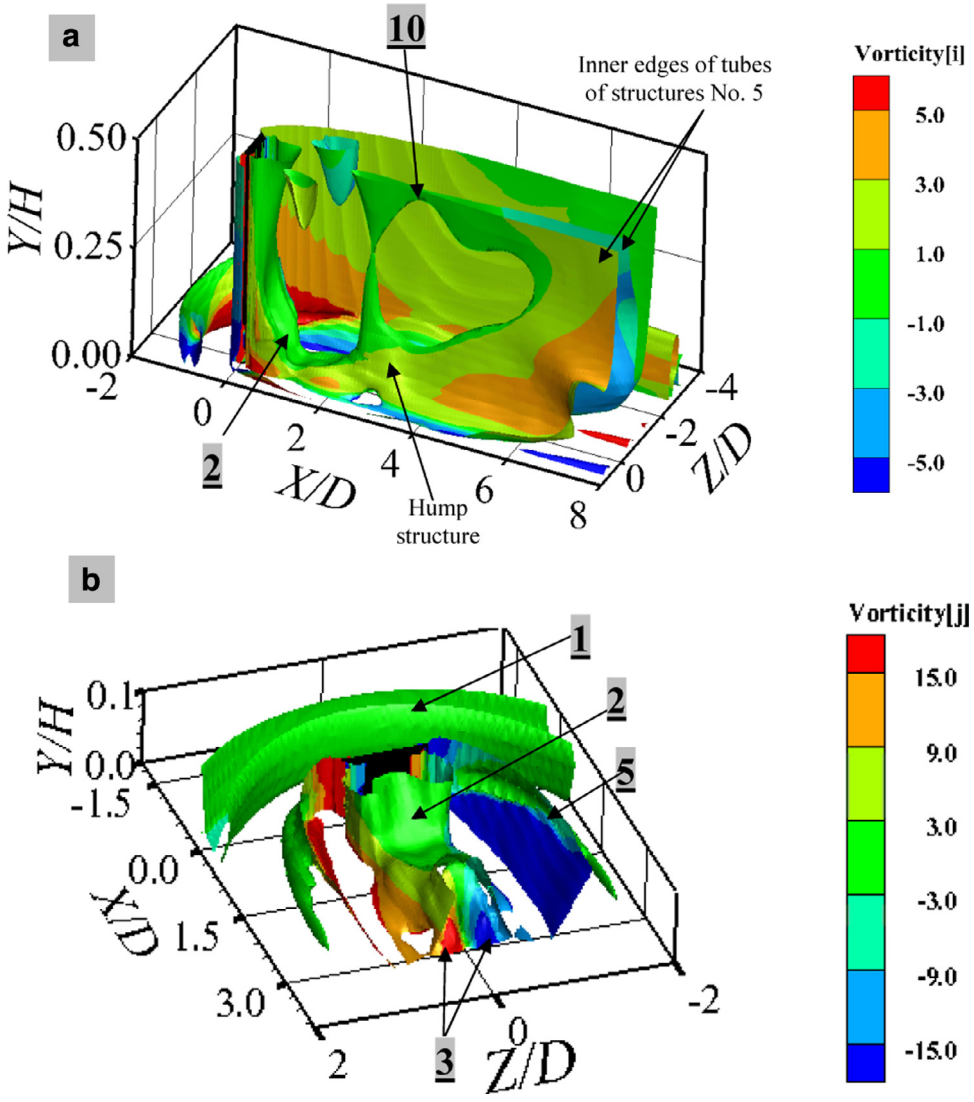

Fig. 8. Time-averaged structures extracted from specific regions in Fig. 5, the structures are shaded with; (a) *X*-vorticity; (b) *Y*-vorticity.

sense as No. 6. A secondary current (Maheo, 1999) near the free surface can be attributed to the structures marked as No. 9 in Fig. 5. A secondary current is an outward flow from the wake and it is normal to the main stream. As in the case of structures No. 8, the structures marked as No. 9 diminish as the upward flow weakens downstream. In Fig. 7, the λ_2-criterion is able to capture the structures marked as No. 1 and 8 at the near-bed locations. However, it fails to independently capture the structures marked as No. 9 near the free surface as they may be amalgamated with the structures marked as No. 6.

Fig. 8 shows specific regions in the flow field, which are extracted from Fig. 5, to illustrate other embedded structures that were not previously visible. The extent of the extracted regions is shown in Fig. 8a and b. In the transverse direction of Fig. 8a, the structures are cut with planes at $Z/D = 0.5$ and $Z/D = -3.2$, for better clarifications of the embedded structures. The outer edges of the tube structures marked as No. 5 in Fig. 5 roll inwards at streamwise location $X/D = 8.0$, transporting the fluid particles into the wake core. The inner edges of the tube structures No. 5 approach each other towards the wake central plane as shown in Fig. 8a. A new structure marked as No. 10 (joined structure) is generated in the clearance between the structures No. 5 in the streamwise location $3.0 < X/D < 6.0$. This horizontally oriented structure plays a role to bridge both vertical tubes of structures No. 5. Ultimately, and as the inner edges approach further, they are joining at the location $X/D \approx 2.5$ as shown in Fig. 8a. At the joining region, the interaction between the structures No. 5 and the bed produces a distinct hump as shown in Fig. 8a. This hump structure conceals a pair of structures, which are residing near the bed as shown in Fig. 8b. A horizontal section through these structures shows a pair of 2-D counter-rotating inward spiralling patterns (vertically oriented) with stable foci (Perry and Steiner, 1987). These patterns resemble the owl face of the first kind (Nasif et al., 2015; Akilli and Rockwell, 2002). A vertical section through these structures also shows a pair of 2-D counter-rotating inward spiralling patterns (streamwise-oriented) with stable foci (Perry and Steiner, 1987). The 3-D roll-up structure marked as No. 2 in Fig. 8 and Fig. 4a, which is a horizontally oriented structure, emerges from the clearance between the structures No. 3 and rolls up upstream towards the bluff body. This structure is similar to structure No. 10, which plays a role to connect both vertical tubes of structure No. 5.

A better understanding of the structures that emerge from underneath the hump of the joining region in Fig. 8a can be obtained by extracting the streamtraces at three perpendicular planes through this region as shown in Fig. 9. In this figure, the streamtraces are extracted in a horizontal plane close to the bed

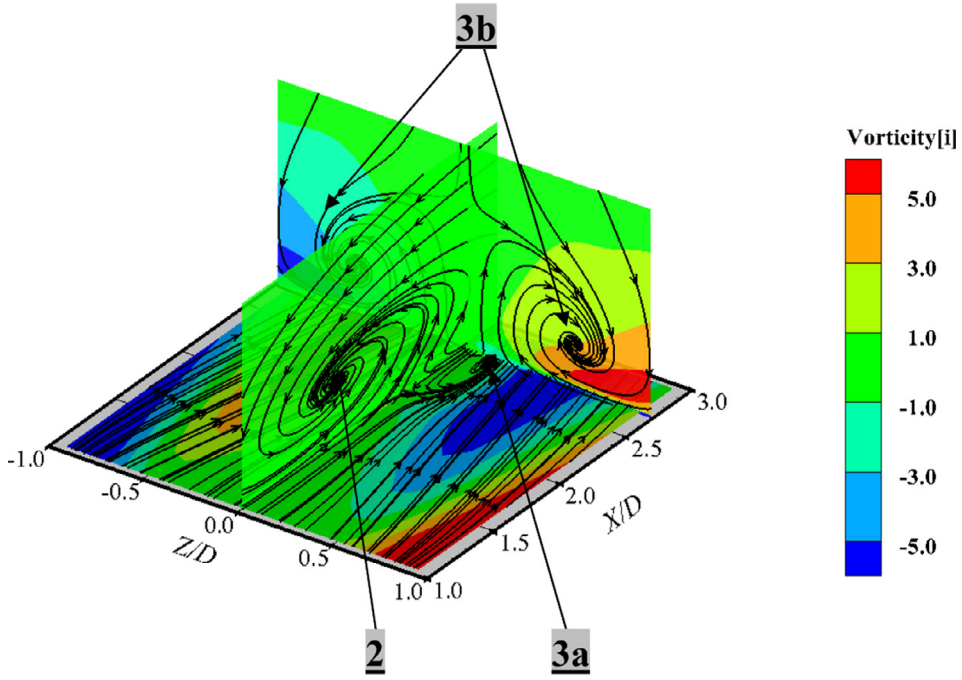

Fig. 9. Section planes through the three-dimensional bulge (shown in Fig. 8b); the streamtraces in the figure are shaded by *X*-vorticity vector.

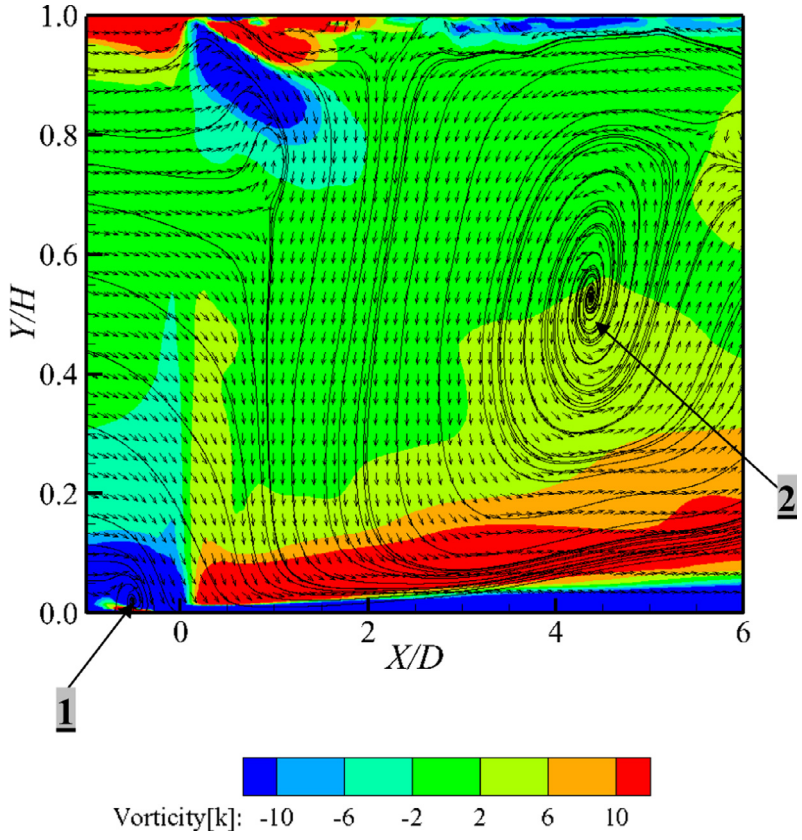

Fig. 10. Time-averaged streamtraces superimposed by contours of the mean *Z*-vorticity extracted at vertical plane $Z/D = 0.75$.

at $Y/H \approx 0.02$, a vertical plane at $X/D \approx 2.75$, and in the vertical plane through the wake central plane ($0 < Y/H < 0.5$). It is obvious from Fig. 9 that the three patterns marked as No. 2, 3a and 3b, are all originating from the near-bed region. The pattern 3b, which is formed by a cross-section through structure No. 3, initiates from the streamwise location at $X/D \approx 2.0$, stretches and rises from the bed as it moves downstream and finally diminishes at $X/D > 6.0$. These structures are very similar to the structures near the surface (No. 9 in Fig. 7) as both are transporting the fluid particles from the wake core to the outer surroundings; one from the locations at the near-bed and the other from the locations at near-free surface.

Finally, Fig. 10 shows the streamtraces superimposed by the Z-vorticity extracted at vertical plane $Z/D = 0.75$. It is clearly shown in this figure that the fluid particles leave the centre plane of the wake (via the streamwise component of structure No. 3, marked as No. 3b in Fig. 9) and merges into the outer stream flow. Contrary to the wake central plane, the downward flow is dominant in the outer region of the near wake. The positive directed velocity is also observed at near-bed locations due to the bed effect. The lateral pattern in Fig. 10 represents a section through the 3-D roll-up structure (marked as No. 2) in Fig. 8a. This structure extends laterally from the wake central plane and diminishes at $|Z/D| > 0.8$. The structure lifts away from the bed and shifts downstream as one moves outwards from the wake central plane (these details are not shown here).

Conclusions

The present study is dedicated toward a detailed characterization of the fluid structures in the mean flow field of the shallow wake. The computational study was carried out using the finite volume technique to examine the vortical structures obtained by the λ_2-criterion. Both the volume of fluid method and rigid-lid assumption are employed to verify the effect of the chosen approach on the fluid structures. The three-dimensional feature of the shallow-wake flow is apparent in this study with the determination of new fluid structures not hitherto observed in these flows. The conclusions can be summarized as follows:

- Although the rigid-lid assumption is computationally inexpensive in comparison with the volume of fluid method, the latter approach has a significant impact on the structures' development at the near-surface location in the far-wake and on the streamtraces in front of the bluff body. The numerical results are more realistic with the volume of fluid method.
- Due to the decline in the magnitude of the mean velocity, the kinetic energy required to sustain the large-scale structures in the far-wake is not sufficient to maintain and retain these structures as they are in the near-wake. As a result, the interaction between the structures and the bed is weakened. This will adjust the structures' orientation from vertical (normal to the flow stream) to horizontal (parallel to the flow stream). Therefore, new structures are generated in the far-wake.
- The upward flow is dominant in the entire wake central plane. However, the downward flow is dominant in the outer regions of the near-wake. The recirculation region (region of negative velocity) is absent in the near-bed region due to the bed effect.
- The entrainment process in the far-wake region acts to stretch the horseshoe vortex inwards towards the wake central plane. As a result, new tube structures are established near the bed in the wake inner region, close by and parallel to the horseshoe legs. These tube structures have the same rotation sense as the horseshoe vortex.
- Due to the interaction between the large-scale structures and the bed in the near-wake, distinctive structures are generated near the bed. A horizontal section through these structures shows a pair of 2-D counter-rotating inward spiralling patterns (vertical-oriented) resembling the owl face of the first kind. A vertical section through these structures shows a pair of 2-D counter-rotating inward spiralling patterns (streamwise-oriented) with stable foci. The latter one transports the fluid particles from the wake inner region to the outer mean stream flow.
- Other structures are found near the free surface to transport the fluid particles from the wake core to the outer region in the far-wake. These structures have a counter rotational sense and are generated at the wake boundaries due to the impinging of the upward moving fluid particles through the wake central plane with the free surface.

References

Akilli, H., Rockwell, D., 2002. Vortex formation from a cylinder at shallow flow. Phys. Fluids 14, 2957–2967.

CD-adapco, STAR-CCM+ V8.06.007, User Manual, 2013.

Chakraborty, P., Balachandar, S., Adrian, R.J., 2005. On the relationships between local vortex identification schemes. J. Fluid Mech. 535, 189–214.

Chen, D., Jirka, G.H., 1995. Experimental study of plane turbulent wakes in a shallow water layer. Fluid Dyn. Res. 16, 11–41.

Gupta, R., Kumar, S., Banerjee, S., 1994. Characteristics of attached vortices in free surface channel flows. In: 12th US National Congress of Applied Mechanics. Washington, USA.

Hirt, C.W., Nichols, B.D., 1981. Volume of fluid (VOF) method for the dynamics of free surfaces. J. Comput. Phys. 39, 201–225.

Hunt, J.C.R., Graham, J.M.R., 1978. Free stream turbulence in near plane boundaries. J. Fluid Mech. 84, 209–235.

Jeong, J., Hussain, F., 1995. On the identification of a vortex. J. Fluid Mech. 285, 69–94.

Jirka, G.H., Uijttewaal, W.S.J., 2004. Shallow Flows: Research Presented at the International Symposium on Shallow Flows, Delft, Netherlands, 2003. Taylor & Francis, London.

Leonard, B.P., 1991. The ULTIMATE conservative difference scheme applied to unsteady one-dimensional advection. Comput. Methods Appl. Mech. Eng. 88, 17–74.

Maheo, P., 1999. Free Surface Turbulent Shear Flow (Ph.D. dissertation). California Institute of Technology, CA, USA.

Menter, F.R., 1993. Zonal two-equation k-ω turbulence models for aerodynamic flows. AIAA Paper 2906.

Menter, F.R., 1994. Two-equation eddy-viscosity turbulence models for engineering applications. AIAA J. 32, 1598–1605.

Menter, F.R., Kuntz, M., 2004. Adaptation of eddy-viscosity turbulence models to unsteady separated flow behind vehicles. The Aerodynamics of Heavy Vehicles: Trucks, Buses, and Trains, 19. Springer, Berlin, Heidelberg, Germany, pp. 339–352.

Muzaferija, S., Peric, M., Sames, P., Schelin, T., 1998. A two-fluid Navier-Stokes solver to simulate water entry. In: 22nd Symposium on Naval Hydrodynamics. Washington, D.C., USA, pp. 638–651.

Nasif, G., Barron, R.M., Balachandar, R., 2014. DES evaluation of near-wake characteristics in a shallow flow. J. Fluids Struct. 45, 153–163.

Nasif, G., Balachandar, R., Barron, R.M., 2015. Characteristics of flow structures in the wake of a bed-mounted bluff body in shallow open channels. J. Fluids Eng. 137, 101207–101207-10.

Pan, Y., Banerjee, S., 1995. Numerical study of free surface turbulence in channel flow. Phys. Fluids 7, 1649–1663.

Patil, P.P., Tiwari, S., 2008. Effect of blockage ratio on wake transition for flow past square cylinder. Fluid Dyn. Res. 40, 753–778.

Perry, A.E., Steiner, T.R., 1987. Large-scale vortex structures in turbulent wakes behind bluff bodies: 1. Vortex formation process. J. Fluids Eng. 174, 233–265.

Rubinat, M., 2007. Procedure for the Identification of Coherent Structures in Oscillatory and Pulsating Flows Over a Wavy Bottom (Master thesis). University of North Carolina, NC, USA.

Singha, A., Balachandar, R., 2010. An assessment of the literature and recent development on the shallow wake in an open channel flow. Adv. Civil Eng. 2010. Article ID 969407, 12 pages. doi: 10.1155/2010/9694

Singha, A., Balachandar, R., 2011a. Coherent structure statistics in the wake of a sharp-edged bluff body placed vertically in a shallow channel. Fluid Dyn. Res. 43, 055504.

Singha, A., Balachandar, R., 2011b. Structure of wake of a sharp-edged bluff body in shallow channel flow. J. Fluids Struct. 27, 233–249.

Shen, L., Triantafyllou, G.S., Yue, D.K.P., 2000. Turbulent diffusion near a free surface. J. Fluid Mech. 407, 145–166.

Travin, A., Shur, M., Strelets, M.M., Spalart, P.R., 2002. Physical and numerical upgrades in the detached-eddy simulation of complex turbulent flows. Advances in LES of Complex Flows. Springer, Netherlands, pp. 239–254.

Walker, D.T., Leighton, R.I., Garza-Rios, L.O., 1996. Shear free turbulence near a flat free surface. J. Fluid Mech. 320, 19–51.

Wang, H.F., Zhou, Y., 2009. The finite-length square cylinder near wake. J. Fluid Mech. 638, 453–490.

White, L., Beckers, J.M., Deleersnijder, E., Legat, V., 2006. Comparison of free surface and rigid-lid finite element models of barotropic instabilities. Ocean Dyn. 56, 86–103.

Versteeg, H.K., Malalasekera, W., 1995. An Introduction to Computational Fluid Dynamics: the Finite Volume Method, 2nd ed. Pearson Education Ltd., Harlow, UK.